

Vorticity Dynamics and Flow Statistics Near the Edge of High-Speed Multi-Stream Jets

A. Adam*, D. Papamoschou†, J. Xiong‡ and F. Liu§

University of California, Irvine, Irvine, CA, 92697, USA

We investigate the vorticity dynamics and flow statistics near the edge of multi-stream, high-speed jets for the purpose of developing linear surface-based models for the noise source. Those models would be informed by low-cost, Reynolds-Averaged Navier-Stokes (RANS) computations of the flow field. The study encompasses two triple-stream jets, one coaxial and the other eccentric, and a single-stream round jet. Large Eddy Simulations (LES) validate RANS-based models for the convective velocity U_c of the noise-generating turbulent eddies in the jet flow. In addition, the LES results help define a “radiator surface” on which the jet noise source model would be prescribed. The radiator surface is located near the boundary between the rotational and irrotational fields and is defined as the surface on which the U_c distribution, obtained from space-time correlations of the pressure, matches that inferred from the RANS model. This surface overlaps with a band of negative skewness of the pressure. Examination of the instantaneous vorticity field shows vortices peeling off from the main flow and migrating towards the radiator surface outside of which their strength vanishes. The vortical events near the radiator surface help explain the negative pressure skewness. The edge of the mean vorticity is nearly coincident with the radiator surface, which suggests a straight-forward RANS-based criterion for locating this surface.

Nomenclature

a	=	speed of sound
A	=	duct exit area
D	=	nozzle exit diameter
\hat{D}	=	equivalent diameter (Eq. 1)
g	=	principal component of the Reynolds stress
M	=	fully-expanded Mach number
M_c	=	convective Mach number
p	=	pressure
r	=	radial coordinate from jet centerline
R	=	space-time correlation
Sk	=	skewness
t	=	time
U	=	fully-expanded velocity
\hat{U}	=	equivalent velocity (Eq. 2)
U_c	=	convective velocity
u, v, w	=	velocity components in Cartesian coordinate system
W	=	annulus width
x, y, z	=	Cartesian coordinates, with y on plane of symmetry
ϕ	=	azimuthal angle relative to downward vertical
ω	=	vorticity vector

*PhD student, Department of Mechanical and Aerospace Engineering, AIAA Member

†Professor, Department of Mechanical and Aerospace Engineering, Fellow AIAA

‡Associate Specialist, Department of Mechanical and Aerospace Engineering, AIAA Member

§Professor, Department of Mechanical and Aerospace Engineering, Fellow AIAA

Subscripts

j	=	single-stream jet
p	=	primary stream
s	=	secondary stream
t	=	tertiary stream
∞	=	ambient

Acronyms

LES	=	Large Eddy Simulation
NTR	=	nozzle temperature ratio
OSPS	=	outer surface of peak stress
RANS	=	Reynolds-Averaged Navier Stokes

I. Introduction

The research effort described here targets the development of low-order predictive models for the noise emission of complex multi-stream turbulent jets associated with the exhaust of advanced turbofan engines. For these models to be effective as design tools, they need to rely entirely on Reynolds-Averaged Navier Stokes (RANS) solutions of the flow field. With reasonable computational resources, RANS solutions can be obtained within hours. High-fidelity methods such as large eddy simulation (LES), coupled with surface integral methods, have evolved to the point where they can yield accurate noise predictions,¹ but entail very large computational resources, long turnaround times, and enormous data sets. However, LES can shed light on physical mechanisms that inform the low-order model, and is used in this context here.

The focus of this investigation is on three-stream jets at conditions relevant to variable-cycle engines for supersonic transports. Henderson² surveyed the acoustics of a three-stream configuration where the core and bypass streams are internally mixed upstream of the tertiary exit; the added tertiary flow reduced high-frequency noise at broadside and peak jet noise angles. Henderson *et al.*³ conducted acoustic experiments and flow field simulations of jets from three-stream nozzles with axisymmetric and offset configurations for the tertiary stream. The offset tertiary stream reduced noise along the thick side of the jet when the core flow was operating at supersonic conditions. Henderson and Wernet⁴ investigated the mean flow field and turbulence characteristics of externally mixed, convergent three stream nozzles using stereo particle image velocimetry. Huff *et al.*⁵ assessed the capability of three-stream, offset duct configurations to meet Chapter 14 noise regulations. Our research group has conducted extensive parametric studies of offset three-stream nozzle concepts and has identified promising quiet configurations that involve duct asymmetry in combination with a wedge-shaped fan flow deflector.^{6,7}

RANS-based predictive models for multi-stream jets have focused on the acoustic analogy coupled with methods to account for the refraction by the mean flow. Including the refraction is particularly critical for asymmetric configurations with azimuthal directivity of the acoustic emission. Construction of the related Green's functions involves complex numerical procedures.⁸ Application to three-stream jets with offset tertiary duct has shown initial promise,³ although the asymmetry in the modeled azimuthal directivity was weaker than the experimental one. More recently, Papamoschou⁹ has proposed an alternative methodology where the azimuthal influence is induced by special forms of the space-time correlations of the Lighthill stress tensor. This work has also underscored the importance of properly modeling the convective velocity U_c of the turbulent eddies that dominate sound production.⁹ Specifically, sound emission is thought to be strongly influenced by the dynamics of the outer shear layer of the multi-stream jet. In a time-averaged sense, the action of the eddies in the outer shear layer is represented by the local peak of the Reynolds stress, resulting in the definition of the outer surface of peak stress (OSPS). The mean axial velocity on this surface is set to represent U_c , and the axial convective Mach number, which controls the radiation efficiency, is defined accordingly.

An alternative to the volumetric models for the noise source used in acoustic analogy are surface-based models where the noise source is prescribed on a surface surrounding the jet flow, typically located in the linear pressure field.^{10,11} In principle, such models allow not only propagation but also scattering predictions (e.g., from airframe surfaces) using well-established techniques like the boundary element method;^{12,13} thus, they have the capacity to address the acoustics of propulsion-airframe integration. In addition, they may

simplify the treatment of the azimuthal directivity from asymmetric jets noted above. The conceptual application of this approach to multi-stream jets is depicted in Fig. 1. The source is prescribed as random partial fields on a “radiator surface” at the boundary between the inner nonlinear rotational flow field and outer linear pressure field. It is on this surface that the linear pressure distribution reflects the “footprint” of the turbulence, and in particular the coherent structures that dominate mixing and noise generation.^{14,15} Each partial field is envisioned to be an amplitude modulated traveling wave with finite axial and azimuthal scales, reflecting the wavepacket nature of jet noise that has been the subject of numerous studies.^{16–20} As with the volumetric approach, modeling of the convective velocity U_c on the radiator surface is a critical element of the predictive scheme. It is desired to inform this decision using the RANS solution and particularly the convective velocity modeled as the mean axial velocity on the OSPS, using the principal ideas in Ref. 9.

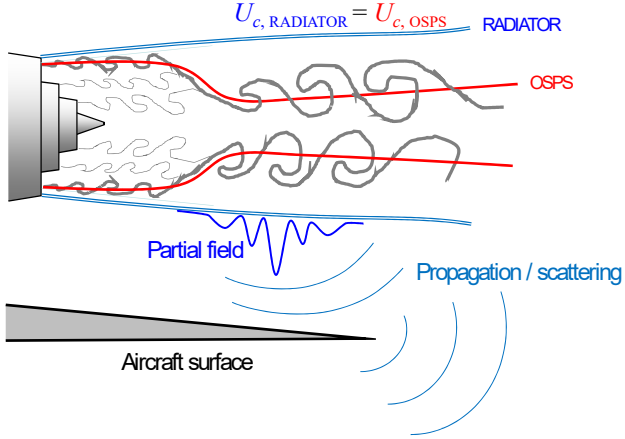


Figure 1: Basic elements of surface-based modeling of the noise source of multi-stream jets.

In this vein, the radiator surface is defined here as the surface at the edge of the jet where the convective velocity, computed directly from space-time correlations, equals the RANS-inferred convective velocity on the OSPS, as shown in Fig. 1. We call this criterion “ U_c -match.” Earlier work on an axisymmetric three-stream jet showed favorable comparisons between the LES- and RANS-based predictions of the OSPS and associated convective velocity distribution; the U_c -match concept for the definition of the radiator showed promise as well.²¹ Here we extend the prior work to asymmetric jets and include a single-stream round jet for reference. Some of the earlier results for the three-stream axisymmetric jet are included for completeness. Importantly, we ask the question whether the radiator surface can be located, at least approximately, from knowledge of the RANS flow variables alone. To this end, we explore instantaneous and statistical aspects of the vorticity and pressure, with emphasis on events near the edge of the jet. Important insights are gained as to the imprint of vortical structures in jet flow on the radiator surface.

II. Jet Flows

We analyze the flow fields of three high-speed turbulent jets: two triple-stream configurations and one single-stream flow. The three-stream jets are labeled AXI04U and ECC09U, and have been the subject of earlier works.^{7,21} Their designs are depicted in Fig. 2. The subscripts p , s and t refer to the primary (inner), secondary (middle) and tertiary (outer) streams, respectively. Both three-stream nozzles share the same area-based exit diameter of the primary duct $D_{p,\text{eff}} = 13.33$ mm. Their secondary-to-primary and tertiary-to-primary area ratios are also common, $A_s/A_p = 1.44$ and $A_t/A_p = 1.06$. Nozzle AXI04U is an axisymmetric design, while nozzle ECC09U has an eccentric tertiary duct with width whose azimuthal distribution $W_t(\phi)$ is included in Fig. 2. Nozzle AXI04U has a tertiary exit diameter $D_t = 38.1$ mm. Compared to nozzle AXI04U, nozzle ECC09U has a wider tertiary duct in the angular segment $-110^\circ \leq \phi \leq 110^\circ$. On the top of the nozzle, the tertiary duct closes completely by means of a wedge-shaped deflector of side length $L = 2.1 D_{p,\text{eff}}$ and half-angle $\delta = 18^\circ$. The single-stream jet, labeled M09, issues from a convergent nozzle with exit diameter $D_j = 0.0218$ m.

The jets are studied using a Cartesian coordinate system where x is the axial direction (along the jet centerline) and y is the transverse direction on the symmetry plane. The origin of the coordinate system is placed at the tip of the plug of the three-stream nozzles and at the center of the exit plane of the single-stream nozzle.

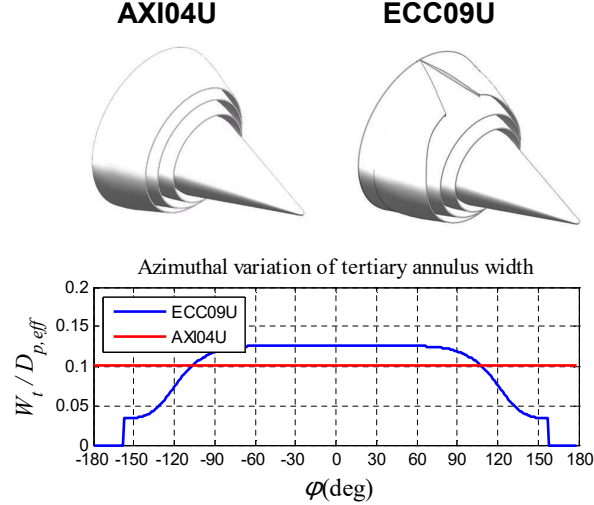


Figure 2: Exit geometry and azimuthal variation of the tertiary annulus width for the three-stream nozzles of this study.

The flow conditions are listed in Table 1. Jets AXI04U and ECC09U have a common set point that represents typical exhaust conditions for a supersonic turbofan engine.⁷ Jet M09 is cold at high-subsonic conditions. In the table, NTR denotes the nozzle temperature ratio, M denotes the fully-expanded Mach number, and U is the fully-expanded velocity. For the three-stream jets, the Reynolds number based on the primary exit conditions and $D_{p,\text{eff}}$ is 1.8×10^5 . For jet M09, the Reynolds number based on D_j is 3×10^5 .

Nozzle	Stream	NTR	M	U (m/s)
AXI04U and ECC09U	Primary	3.38	1.07	590
	Secondary	1.34	1.06	370
	Tertiary	1.24	0.81	282
M09		1.00	0.90	286

Table 1: Flow conditions.

In order to establish trends that are applicable to single- and multi-stream jets, we use equivalent length and velocity scales as follows. The equivalent diameter of the multi-stream jet is based on the total exit cross-sectional area:

$$\hat{D} = \sqrt{\frac{4}{\pi}(A_p + A_s + A_t)} = 0.0249 \text{ m} \quad (1)$$

The equivalent velocity is based on the mass average

$$\hat{U} = \frac{\dot{m}_p U_p + \dot{m}_s U_s + \dot{m}_t U_t}{\dot{m}_p + \dot{m}_s + \dot{m}_t} = 435 \text{ m/s} \quad (2)$$

where \dot{m} denotes mass flow of each individual stream. Obviously, for the single-stream jet $\hat{D} = D_j$ and $\hat{U} = U_j$.

III. Computational Details

The computational effort encompassed Reynolds-Averaged Navier Stokes (RANS) solutions and Large Eddy Simulations (LES). Jets AXI04U and ECC09U were investigated using both RANS and LES. Jet M09 was studied using LES only. The simulations were performed at the conditions of Table 1 and the Reynolds numbers listed in the previous section.

The computational fluid dynamics code is known as PARCAE²² and solves the unsteady three-dimensional Navier-Stokes equations on structured multiblock grids using a cell-centered finite-volume method. Information exchange for flow computation on multiblock grids using multiple CPUs is implemented through the MPI (Message Passing Interface) protocol.

In the RANS solutions the Jameson-Schmidt-Turkel dissipation scheme²³ and the Shear Stress Transport (SST) turbulence model of Menter²⁴ were used. The RANS solver has been used in past research on dual-stream jets, and its predictions have been validated against mean velocity measurements performed at UCI for dual-stream jets.²⁵

For the LES, the PARCAE solver uses implicit backward three-layer second-order time integration with explicit five stage Runge-Kutta dual time stepping, residual smoothing, and multigrid techniques for convergence acceleration. The spatial discretization of the inviscid flux is based on the weighted averaged flux-difference splitting algorithm of Roe.^{26,27} The viscous flux is discretized using a second-order central difference scheme. The time-evolving jet flow is simulated using a hybrid RANS/LES approach.²⁸ Near the wall region the Spalart-Allmaras turbulence model²⁹ is used to model the turbulent viscosity, while in the free shear flow the computation relies on the subtle dissipation of the upwind scheme, using the method proposed by Shur *et al.*²⁷

To aid convergence, the RANS and LES simulations were conducted with a freestream Mach number of 0.05, or freestream velocity of 17 m/s.

The computations encompassed both the internal nozzle flow as well as the external plume. For each nozzle stream, uniform total pressure and total temperature were specified at the inlet surface corresponding to the respective perfectly expanded exit Mach number. For the ambient region surrounding the nozzle flow, a characteristic boundary condition was defined, and the downstream static pressure was set to the ambient pressure. Adiabatic no-slip boundary condition was specified on all the nozzle walls.

For the RANS solutions, the mesh contained approximately 8 million grid points and extended to $30D_t$ axially and $8D_t$ radially. As the nozzles are symmetric around the $x - y$ plane, only one-half of the nozzle and jet flow were modeled to save computational cost. The LES grid for the three-stream nozzles contained about 44 million grid points and extended to $30D_t$ axially and $15D_t$ radially. Figure 3 displays a portion of the mesh for jet AXI04U, as well as instantaneous vorticity and pressure contours. The LES grid for the single-stream jet contained approximately 7 million points and extended to $60D_j$ axially and $20D_j$ radially.

Limitation of computational resources forced relatively few time steps for the LES. For jets AXI04U and ECC09U, 2000 time steps with $\Delta t = 10 \mu\text{s}$ were used. As a result, some statistics are not fully converged, particularly in the far field. The time steps for jet M09 were 10000 at $\Delta t = 2 \mu\text{s}$.

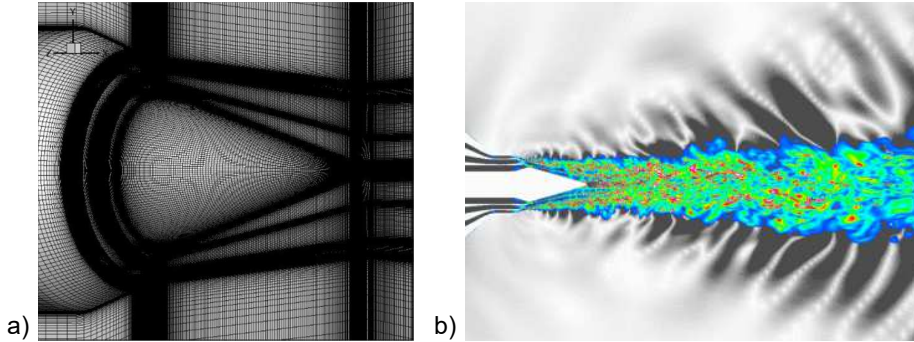


Figure 3: a) Portion of computational mesh and b) instantaneous vorticity (inner) and pressure (outer) contours for jet AXI04U.

IV. Mean Flow Fields

We compare the distributions of the mean axial velocity and the principal component of the Reynolds stress tensor, as computed by both RANS and LES for nozzles AXI04U and ECC09U, and LES for nozzle M09. The significance of the Reynolds stress in the modeling of the noise source in multi-stream jets was emphasized in Ref. 9. Following that work, the magnitude of the principal component of the Reynolds stress is defined as

$$g = | \langle u'q' \rangle | \quad (3)$$

where u' is the axial velocity fluctuation, q' is the transverse velocity fluctuation in the direction of the mean velocity gradient, and $\langle \cdot \rangle$ denotes the time average. For the LES, g is calculated directly from the time-resolved data. For RANS, it is given by

$$g = \nu_T G \quad (4)$$

where ν_T is the turbulent viscosity and G is the magnitude of the mean velocity gradient. For the remainder of the report, g will be loosely referred to as the “Reynolds stress”.

A. Jet AXI04U

Figure 4 plots isocontours of the normalized mean axial velocity, \bar{u}/\hat{U} , on the plane of symmetry of jet AXI04U and compares the RANS and LES predictions. The two flow fields are very similar, with the LES predicting slightly faster spreading and thus moderately smaller primary potential core. It is also noted that the wake from the plug is accentuated in the RANS simulation. The analogous comparisons for the Reynolds stress are presented in Fig. 5. Here we note that the LES results lack sufficient time steps for converging to a smooth distribution for $x/\hat{D} > 10$. Upstream of this region, the comparison between RANS and LES is very good both in terms of levels and shapes of the distributions.

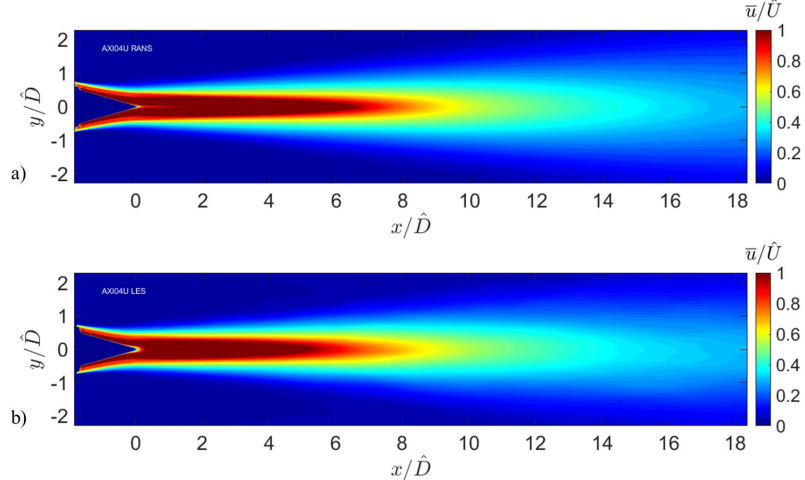


Figure 4: Isocontours of normalized mean axial velocity \bar{u}/\hat{U} on symmetry plane of jet AXI04U. a) RANS and b) LES.

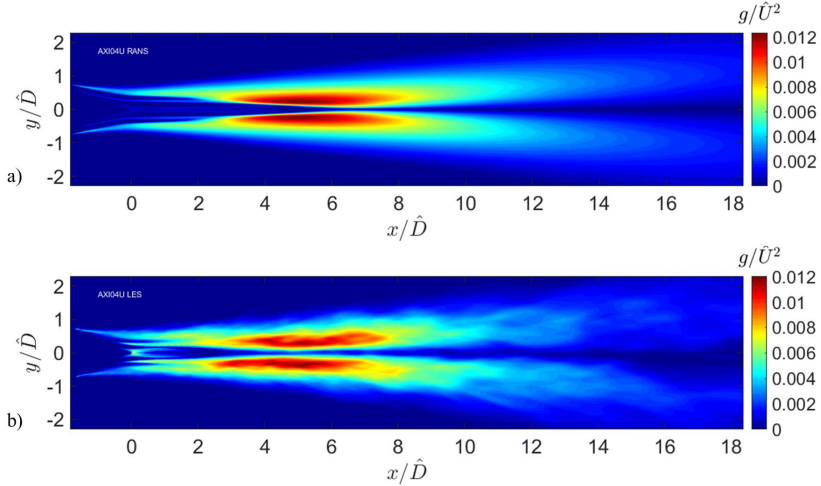


Figure 5: Isocontours of normalized Reynolds stress g/\hat{U}^2 on symmetry plane of jet AXI04U. a) RANS and b) LES.

B. Jet ECC09U

Figure 6 plots isocontours of the normalized mean axial velocity for jet ECC09U. As in the axisymmetric case, we note faster spreading and smaller primary potential core in the LES than in the RANS solution. The asymmetry produced by the eccentricity of the nozzle is evident: there is a significant increase of low-speed flow on the underside of the primary jet. In general terms, the RANS and LES predictions show a good level of similarity. The corresponding comparison of normalized Reynolds stress is shown in Fig. 7. Although it shows a distribution not fully converged to a smooth result, it is reliable enough to draw conclusions for at least $x/\hat{D} \leq 9$. As in the axisymmetric case, the comparisons between RANS and LES show good agreement in terms of levels and distributions. In particular, the large reduction in Reynolds stress on the underside of the jet, and moderate increase on the top side, are matched very well.

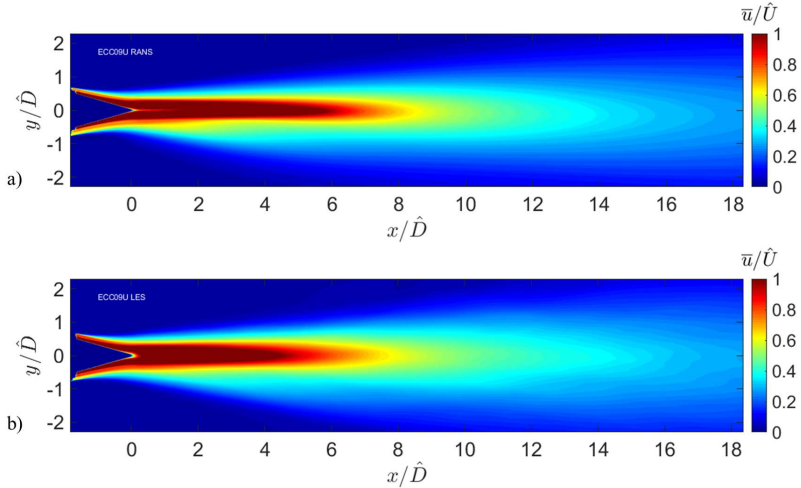


Figure 6: Isocontours of normalized mean axial velocity \bar{u}/\hat{U} on symmetry plane of jet ECC09U. a) RANS and b) LES.

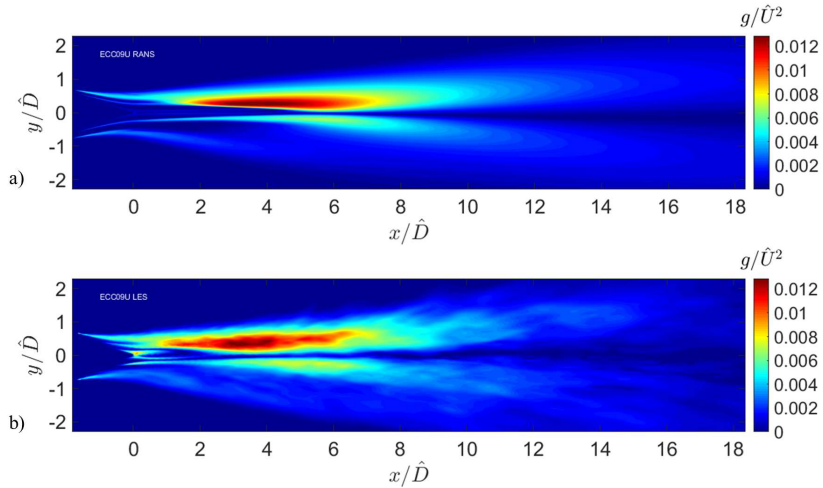


Figure 7: Isocontours of normalized Reynolds stress g/\hat{U}^2 on symmetry plane of jet ECC09U. a) RANS and b) LES.

C. Jet M09

Figures 8 and 9 show the normalized mean axial velocity and Reynolds stress g , respectively, as obtained by LES for jet M09. The distribution of mean axial velocity is consistent with past experiments on this flow.^{30,31} The contours of Reynolds stress in Fig. 9 are also consistent with turbulence measurements in this type of the jet.³² It is notable that the peak level of the normalized Reynolds stress in the axisymmetric three-stream jet AXI04U (Fig. 5) is similar to that in jet M09. This provides support for using the mass-averaged velocity \hat{U} as a normalizing factor when comparing the statistics of single- and multi-stream jets.

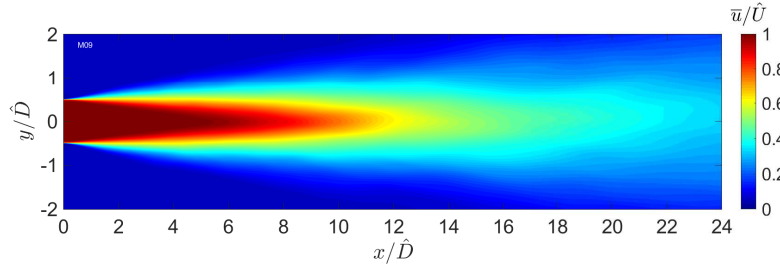


Figure 8: Isocontours of normalized mean axial velocity \bar{u}/\hat{U} on symmetry plane of jet M09.

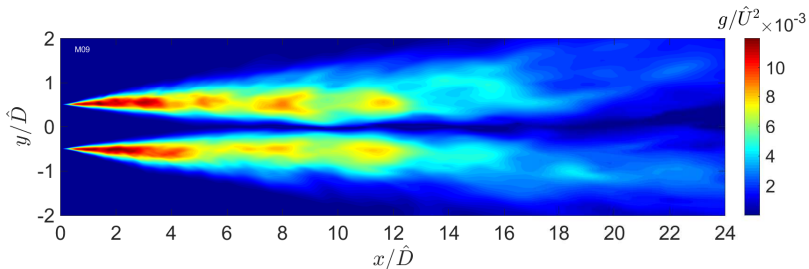


Figure 9: Isocontours of normalized Reynolds stress g/\hat{U}_j^2 on symmetry plane of jet M09.

V. Outer Surface of Peak Stress

In the acoustic analogy model of Ref. 9 it was surmised that, in multi-stream jets, the turbulent eddies in direct contact with the ambient are the principal noise generators. In a three-stream jet these eddies are initially in the tertiary (outer) shear layer, then progressively transition to the secondary and primary shear layers as the tertiary and secondary flows become mixed with the primary flow (Fig. 1). In the context of RANS, the action of those eddies is represented by the statistics on the outer-most peak of the Reynolds stress g , that is, the first peak of g as one approaches the jet radially from the outside towards the inside. This results in the concept of the “outer surface of peak stress” (OSPS), which is thought to be important in the understanding and modeling of multi-stream jet noise. Among the most important properties of the eddies in contact with the ambient is their convective velocity U_c and convective Mach number $M_c = U_c/a_\infty$. The convective Mach number governs the efficiency with which the eddies radiate sound to the far field, it is thus of paramount significance in the modeling. In Ref. 21 we validated the RANS-based model of U_c for jet AXI04U by direct evaluation of U_c from the LES data. Here we extend those comparisons to the asymmetric jet ECC09U; the previous comparisons for jet AXI04U are included for completeness.

The procedure for the detection of the OSPS, outlined in Ref. 21, was applied to all the jets of this study. At a given axial location, the OSPS is detected by constructing rays along the direction of the mean velocity gradient that propagate from the ambient towards the center of the jet; the first maximum of the Reynolds stress g along each ray marks the location of the OSPS.

A. OSPS Based on RANS

For the RANS computations, once the OSPS has been detected, the convective velocity is modeled as the mean axial velocity on the OSPS. Denoting the radius of the OSPS as $r_{\text{OSPS}}(x, \phi)$, the convective velocity is expressed as

$$U_c(x, \phi) = \bar{u}(x, r_{\text{OSPS}}(x, \phi)) \quad (5)$$

Figure 10 plots three-dimensional views of the OSPS for jets AXI04U and ECC09U. The color contours on the surfaces represent the convective Mach number M_c . The OSPS of jet AXI04U experiences a subtle convergence where the tertiary shear layer becomes mixed with the secondary shear layer, followed by a more pronounced convergence where the outer streams become totally mixed with the primary shear. This is followed by a gradual convergence near the end of the primary potential core, downstream of which the OSPS diverges slowly. The peak M_c occurs near the depletion of the outer streams, at $x/\hat{D} \approx 4$. The asymmetry of nozzle ECC09U has a strong effect on the shape of its OSPS. The convergence from tertiary to secondary shear layer, as well as the stronger “collapse” on the primary layer, show a clear dependence on the azimuthal angle ϕ . Those transition points move downstream as ϕ tends to 0° , the downward direction. In addition, in the proximity of $\phi = 0^\circ$, the tertiary shear layer interacts minimally with the secondary and primary layers: it diverges until it vanishes due to spreading. At that point, it stops representing the outer peak of the Reynolds stress and the OSPS collapses on the primary shear layer. This creates the “fin” visible in the downwards direction of Fig. 10b. Overall, the outward deflection of the OSPS on the underside of the jet causes a large reduction in convective Mach M_c . This is key to the noise reduction induced by nozzle ECC09U in the downward direction, as measured in Ref. 7.

B. OSPS Based on LES

The OSPS detection scheme in the LES is analogous to that used for the RANS solution. However, the convective velocity on the surface is computed directly from the normalized axial space-time correlation of the axial velocity fluctuation²¹

$$R_{uu}(x, r, \phi; \xi, \tau) = \frac{\langle u'(x, r, \phi, t) u'(x + \xi, r, \phi, t + \tau) \rangle}{u'_{rms}(x, r, \phi) u'_{rms}(x + \xi, r, \phi)} \quad (6)$$

where rms denotes the root mean square. A similar formulation can be used for R_{pp} , the space-time correlation of p' . Examples of space-time correlations for different axial separations ξ are plotted in Fig. 11. Computation of the convective velocity at a given point involves several space-time correlations at small axial separations. Because each correlation function comprises a discrete set of points, to accurately locate the maximum value of the correlation at axial separation ξ_i a seventh-order polynomial is fitted around the peak

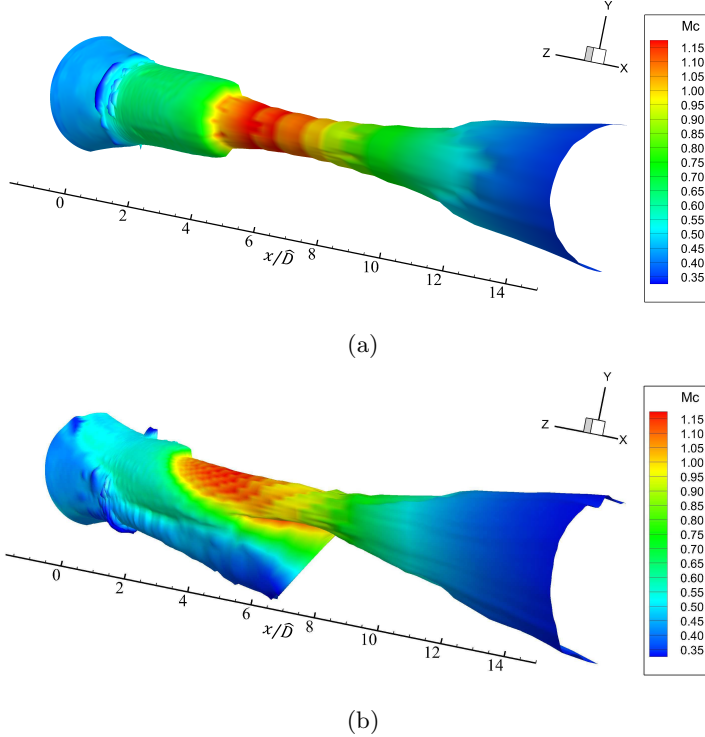


Figure 10: OSPS shape and M_c distribution on OSPS based on RANS solution for jets: (a) AXI04U; (b) ECC09U.

of the correlation curve (dashed lines in Fig. 11). The time separation τ_i corresponding to the maximum value of the polynomial (i.e., the root of the derivative) is then calculated using a Newton-Raphson iteration method. The convective velocity for this axial separation is $U_{c,i} = \xi_i/\tau_i$, and the overall U_c is the average of all $U_{c,i}$ computed from correlations whose peak values exceed 0.4.

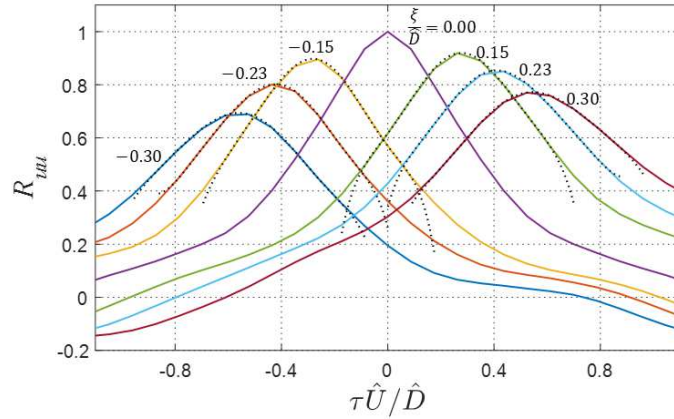


Figure 11: Space-time correlation R_{uu} on the OSPS at $x/\hat{D} = 1.6$ for jet AXI04U. Dashed lines indicate fits by seventh-order polynomials to accurately detect the peak of each correlation.

The resulting OSPS of jets AXI04U, ECC09U and M09 are shown in Fig 12 with color contours of the convective Mach number. The surfaces for the axisymmetric jets AXI04U and M09 were smoothed by azimuthal averaging, a procedure that is not possible for jet ECC09U. As result, the OSPS for jet ECC09U has jagged features due to the limited number of time steps in the LES. Nevertheless, the OSPS shapes and

M_c distributions for jets AXI04U and ECC09U compare favorably to those obtained using RANS in Fig. 10. The OSPLS for jet M09 is approximately a constant-radius cylinder in the potential core region, which extends to $x/\hat{D}=7$. The convective Mach number in this region is $M_c \approx 0.55$, corresponding to $U_c/U_j \approx 0.6$; this is consistent with earlier experimental investigation of this flow.³³

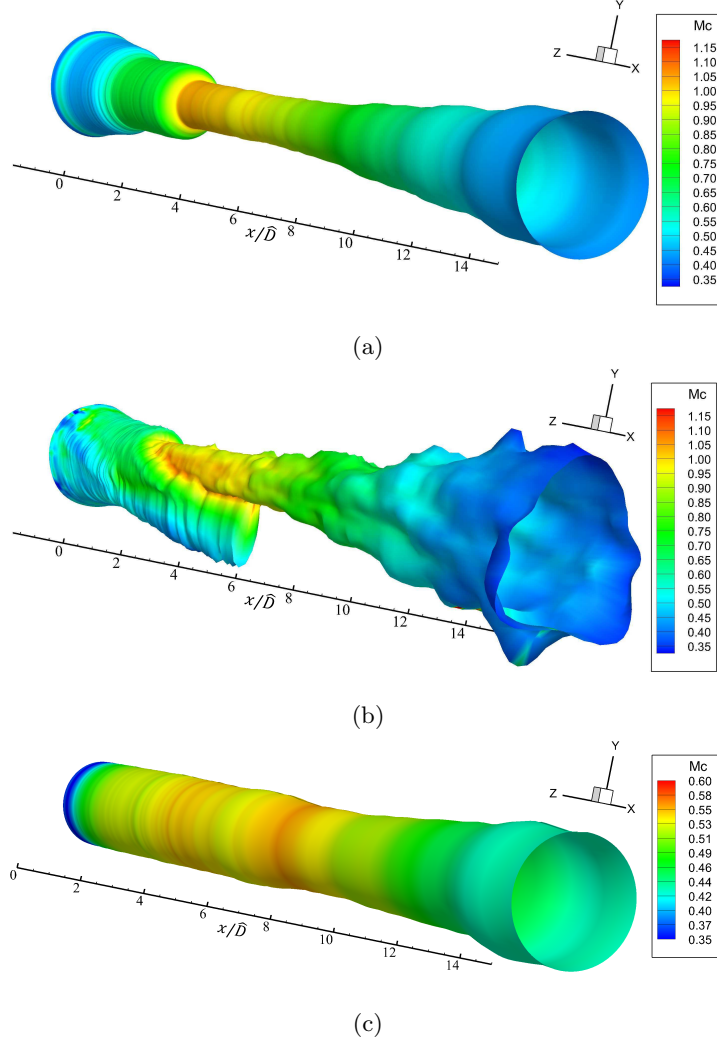


Figure 12: M_c distribution on LES-based OSPLS. (a) Jet AXI04U; (b) jet ECC09U; and (c) jet M09.

C. Comparison of RANS and LES Results on the OSPLS

Having discussed the detection and broad features of the OSPLS, we proceed with detailed comparisons of the geometries and convective velocity distributions obtained by the RANS and LES solutions for the OSPLS of jets AXI04U and ECC09U.

1. Jet AXI04U

Figure 13a plots the radial coordinates of the OSPLS of jet AXI04U as computed by RANS and LES. The two predictions are practically identical up to $x/\hat{D} = 1.5$, with the plot showing clearly the inward transition of the OSPLS from the tertiary to the secondary to the primary shear layer. This transition occurs in LES about one diameter upstream than in RANS. For $x/\hat{D} > 1.5$, the two surfaces are close but the LES result is shifted outward, reflecting the faster spreading of the LES jet.

The comparison of convective velocities on the OSPLS is seen in Fig. 13b. The RANS- and LES-based trends are similar and show an increase in U_c as the most energetic eddies move from the tertiary (low speed)

to the secondary (medium speed), and then to the primary (high speed) shear layer. This is followed by a decline in U_c as the mean velocity decays past the end of the primary potential core. There are moderate quantitative differences between the RANS and LES results, with RANS predicting a peak value of U_c that is about 13% higher than that predicted by LES. This tendency can also be observed when comparing the color contours in Figs. 10 and 12. The maximum U_c takes place at slightly different locations, $x/\hat{D} = 3.5$ for RANS and $x/\hat{D} = 2.25$ for LES, which is explained by the difference in transition to the primary stream in each OSPS.

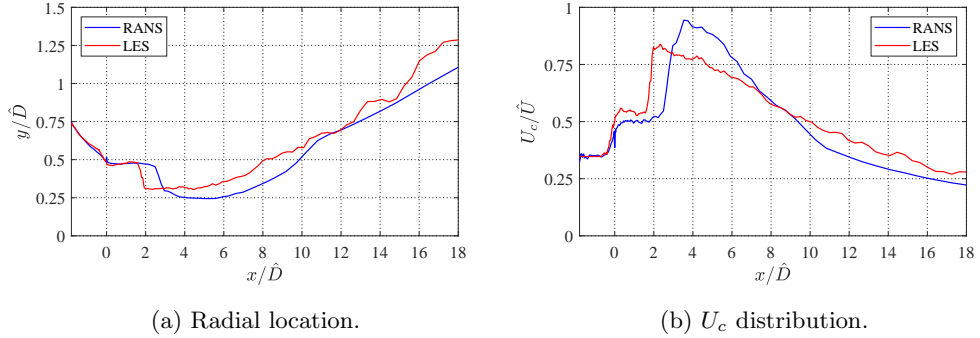


Figure 13: RANS and LES results regarding the OSPS of jet AXI04U.

2. Jet ECC09U

Because of the eccentricity of nozzle ECC09U, the resulting OSPS shape is dependent on the azimuthal angle ϕ . For brevity we only show comparisons for $\phi = 0^\circ$ and $\phi = 180^\circ$. The radial coordinate results for $\phi = 0^\circ$ are plotted in Fig. 14a. There is reasonable agreement between the RANS and LES predictions, both capturing the collapse of the OSPS near $x/\hat{D} = 4$, where the outer shear layer vanishes and the OSPS transitions to the primary shear layer. The axial location of this transition is earlier in the LES than in the RANS solution, consistent with the faster spreading of the LES flow, also seen for jet AXI04U. Downstream of this transition the curves have similar trends, with the LES-based OSPS showing a faster spreading and therefore an outward shift. Past $x/\hat{D} = 13$ the LES-based OSPS loses accuracy due to the lack of convergence of the statistics. Figure 14b compares convective velocities obtained by RANS and LES, using the procedures discussed in Section V.B. The two curves are similar and show a slightly decaying U_c where the OSPS occurs on the outer shear layer. Near $x/\hat{D} = 4$, the collapse of the OSPS to the primary shear layer causes the convective velocity to rise suddenly. The LES predicts a peak U_c value about 12% lower than that obtained from the RANS solution.

Corresponding results for $\phi = 180^\circ$ are shown in Fig. 15. The radial coordinates show similar trends, with an overall faster spreading of the LES jet. Because the tertiary stream is deflected away from the top of the nozzle, the OSPS follows the secondary shear layer, which is quickly merged with the primary shear layer. This transition occurs near $x/\hat{D} = 1.15$ for RANS and around $x/\hat{D} = 0.6$ for LES. Downstream of this transition, the LES result shows a more rapid spreading rate. Despite the location discrepancy seen in Fig. 15a, the RANS- and LES-based convective velocities plotted in Fig. 15b are still in overall agreement. Similarly to jet AXI04U, there is a stepped increment in the convective velocity as the shear layers mix. In this case, because the tertiary flow is deflected such that there are only primary and secondary flows at the top of the jet, only one sudden rise is seen. The rapid jump of the LES-based U_c at $x/\hat{D} \approx -1$ is not considered physical but a result of the numerical difficulty in locating the OSPS very close to the tertiary nozzle lip. The fact that LES predicts the transition from secondary to primary shear layer upstream from RANS naturally leads to an earlier rise of the corresponding convective velocity. After that, the lower LES-based U_c is explained by the faster spreading of the OSPS. Overall, all comparisons provide encouragement that the RANS flow field can yield a fairly accurate convective velocity distribution for the purposes of jet noise modeling.

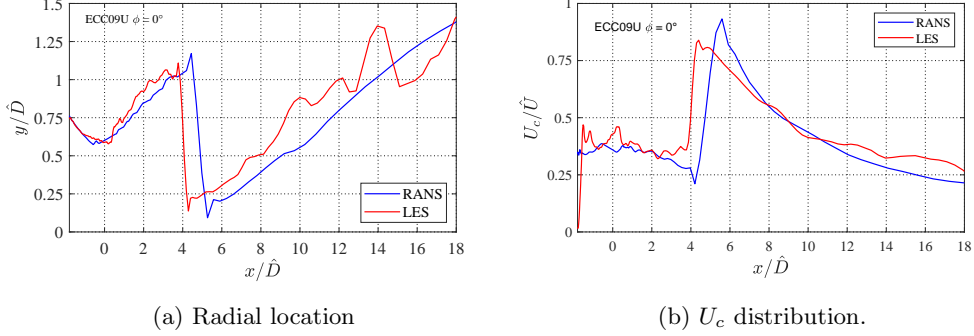


Figure 14: RANS and LES results regarding the OSPLS of jet ECC09U on $\phi = 0^\circ$.

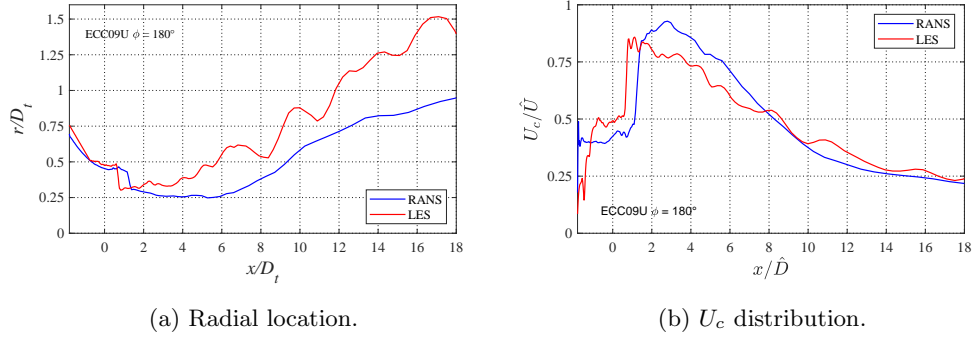


Figure 15: RANS and LES results regarding the OSPLS of jet ECC09U on $\phi = 180^\circ$.

VI. Radiator Surface

The radiator surface is defined as the closest surface to the jet axis on and outside of which the propagation of pressure perturbation is governed by the homogeneous linear wave equation. It is on this surface that a linear model for the jet noise sources, in the form of partial fields,²⁰ could be informed by turbulence statistics computed by low-cost methods such as RANS. As we move away from this surface, the hydrodynamic information is lost rapidly. One of the most important elements of a surface-based source model is the convective velocity U_c .

Previous works of single- and dual-stream jets used a criterion for the location of the radiator surface based on the radial gradient of mean axial velocity, normalized by its peak local value:^{33,34}

$$\frac{\partial \bar{u}/\partial r}{(\partial \bar{u}/\partial r)_{max}} \rightarrow 0 \quad (7)$$

For multi-stream jets, one may select $\partial \bar{u}/\partial r_{max}$ to be the outermost peak of mean velocity gradient, similar to the definition of the OSPLS in Section V. However, a previous study of jet AXI04U found that this definition places the surface too far into the acoustic domain, where the hydrodynamic component is lost.²¹ In the following sections, alternative definitions are considered in the search for a definitive, practical definition based solely on the RANS flow variables. In order to get a deeper understanding of the physics near the edge of the jet, the distributions of convective velocity, vorticity, and skewness of pressure are studied.

A. Distribution of Convective Velocity

As emphasized above, it is desirable that the convective velocity distribution on the radiator surface matches that of the underlying eddies that dominate noise emission. It is then sensible to look for a connection between

the convective velocity distributions on the OSPS and at the edge of the jet. The first thing to determine is whether the LES-based convective velocity should be based on space-time correlations of the axial velocity fluctuation u' or the pressure fluctuation p' . Due to their physical associations, we designate u' -based space-time correlations for the inside of the vortical field, where the turbulent structures affect the velocity of the flow directly; and p' -based correlations for the region near and beyond the the edge of the jet, where we seek the pressure imprint of the vortical eddies. This choice is supported by earlier work on jet AXI04U, which found that the space-time correlations of p' captured the transition from hydrodynamic to acoustic fields better than those based on u' . The space-time correlation of p' , R_{pp} , is defined similarly to R_{uu} in Eq. 6.

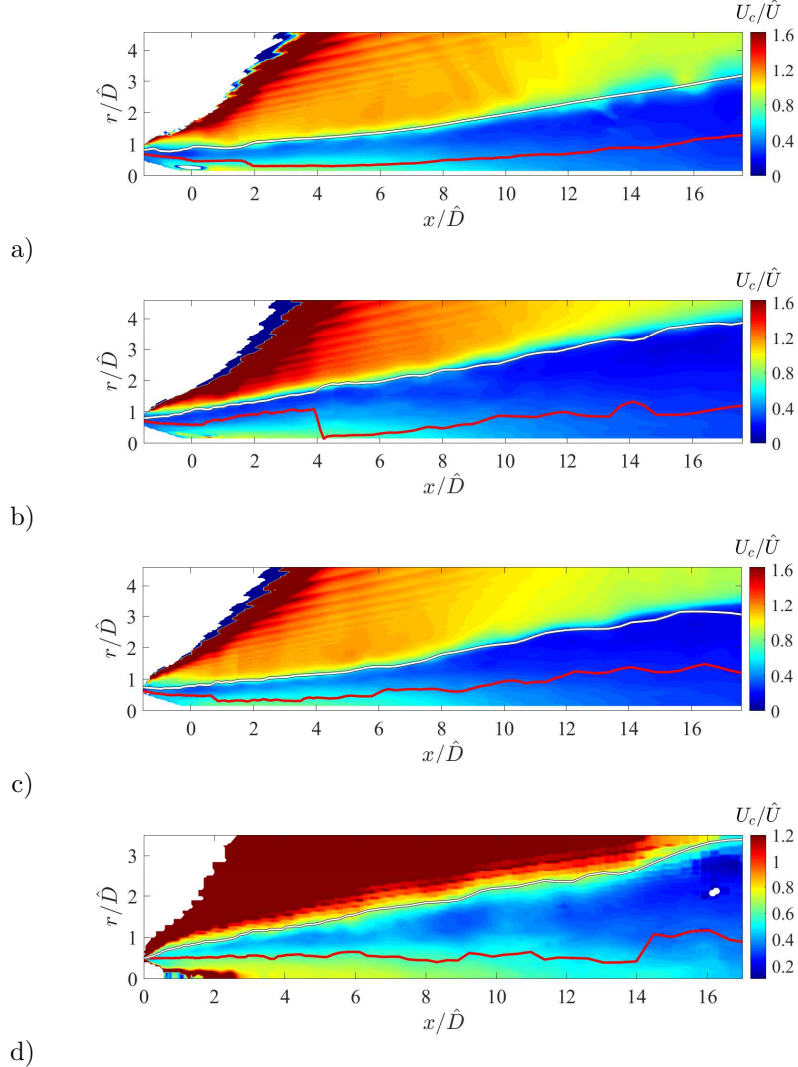


Figure 16: Distribution of normalized convective velocity U_c/\hat{U} as determined by space-time correlations based on p' on the meridional plane of jets: a) AXI04U; b) ECC09U at $\phi = 0^\circ$; c) ECC09U at $\phi = 180^\circ$; d) M09. White lines: radiator surface based on U_c -match criterion; red lines: OSPS surface based on LES.

Figure 16 displays isocontours of R_{pp} -based U_c , normalized by the equivalent velocity \hat{U} , on the meridional planes of jet AXI04U, jet ECC09U at $\phi=0^\circ$ and $\phi=180^\circ$, and jet M09. At a given axial location, U_c has a radial trend whereby it decreases outside the OSPS, reaches a minimum, then rises sharply. The sharp rise is associated with the transition from the hydrodynamic to the acoustic fields. Similar trends were found for jet M09 in Ref. 34. To achieve the aforementioned property of the radiator surface, we search for a surface near the edge of the jet where the U_c distribution matches that on the OSPS. The result are the white lines plotted in Fig. 16. They track very closely the hydrodynamic-acoustic transition of the U_c maps.

The smoothness of the U_c -match lines, and their proximity to the hydrodynamic/acoustic boundary in the R_{pp} -based U_c , suggest that the U_c information on the OSPS is transmitted to the jet rotational/irrotational boundary. It is in fact quite remarkable that a highly distorted OSPS, such as that of jet ECC09U, yields a smooth radiator surface. This provides encouragement that there is a surface, having the desired properties of the radiator surface, on which the RANS-derived convective velocity (on the OSPS) would inform the definition of the partial fields for noise source modeling.

B. Distribution of Vorticity

The main characteristic of the radiator surface is that it is placed at the boundary between the rotational and irrotational fields. It is therefore relevant to study the vorticity distribution as a means of delineating those fields and testing the validity of the U_c -match criterion for defining the radiator surface. We first examine the normalized vorticity fluctuation vector $\omega' \hat{D}/\hat{U}$. Figure 17 plots a snapshot of the third component of the normalized vorticity fluctuation, $\omega'_z \hat{D}/\hat{U}$, on the $x - y$ (symmetry) plane of jet AXI04U. The magnitude of $\omega'_z \hat{D}/\hat{U}$ has a wide dynamic range, approximately $[-35, 35]$, throughout the jet. To accentuate moderate vortical fluctuations near the edge of the jet, a smaller range has been applied to Fig. 17; as a result, many events inside the jet appear saturated in dark red (positive saturation) and white (negative saturation). The plot includes the location of the radiator surface, using the U_c -match criterion. A notable observation is that the radiator surface encloses the vortical events inside the jet, with very scarce events crossing the surface. This feature is seen consistently for all time realizations of this jet as well as jets ECC09U (for all azimuthal angles) and M09. This observation gives credence to the notion that the U_c -match criterion results in a proper placement of the radiator surface. Conversely, we may infer that the footprint of the noise-generating vortical eddies, in terms of their convective velocity, is transmitted on this surface.

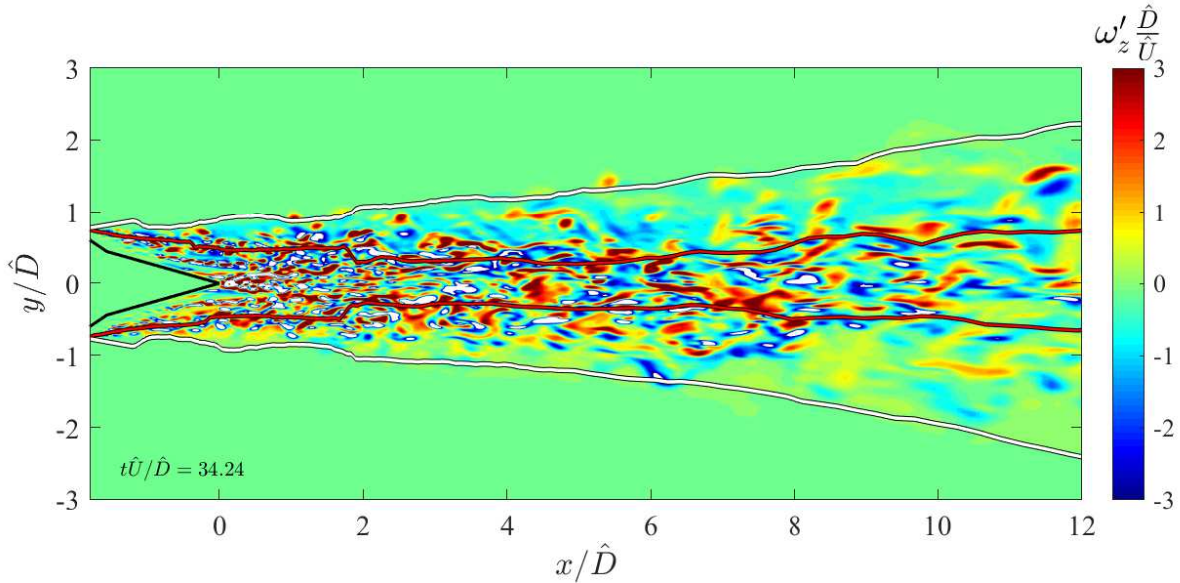


Figure 17: Instantaneous distribution of ω'_z on symmetry plane of jet AXI04U. White line: radiator surface based on U_c -match criterion; red line: OSPS surface based on LES.

C. Location of the Radiator Surface Based on Mean Vorticity

In the search for a RANS-based criterion for the location the radiator surface, we study the mean vorticity distribution of the LES solutions. Figure 18 plots the magnitude of the normalized mean vorticity $|\bar{\omega}| \hat{D}/\hat{U}$ on the symmetry planes of jets AXI04U, ECC09U, and M09. The location of the radiator surface, using the U_c -match criterion, is included. It is again evident that the radiator surface encloses the vortical region of the flow. It is particularly notable that the radiator lines appear to follow the outer contours of the mean

vorticity for jets AXI04U and ECC09U. The same holds for jet M09 except for the region past the end of the potential core, where the radiator line expands at a higher angle than the vorticity contours.

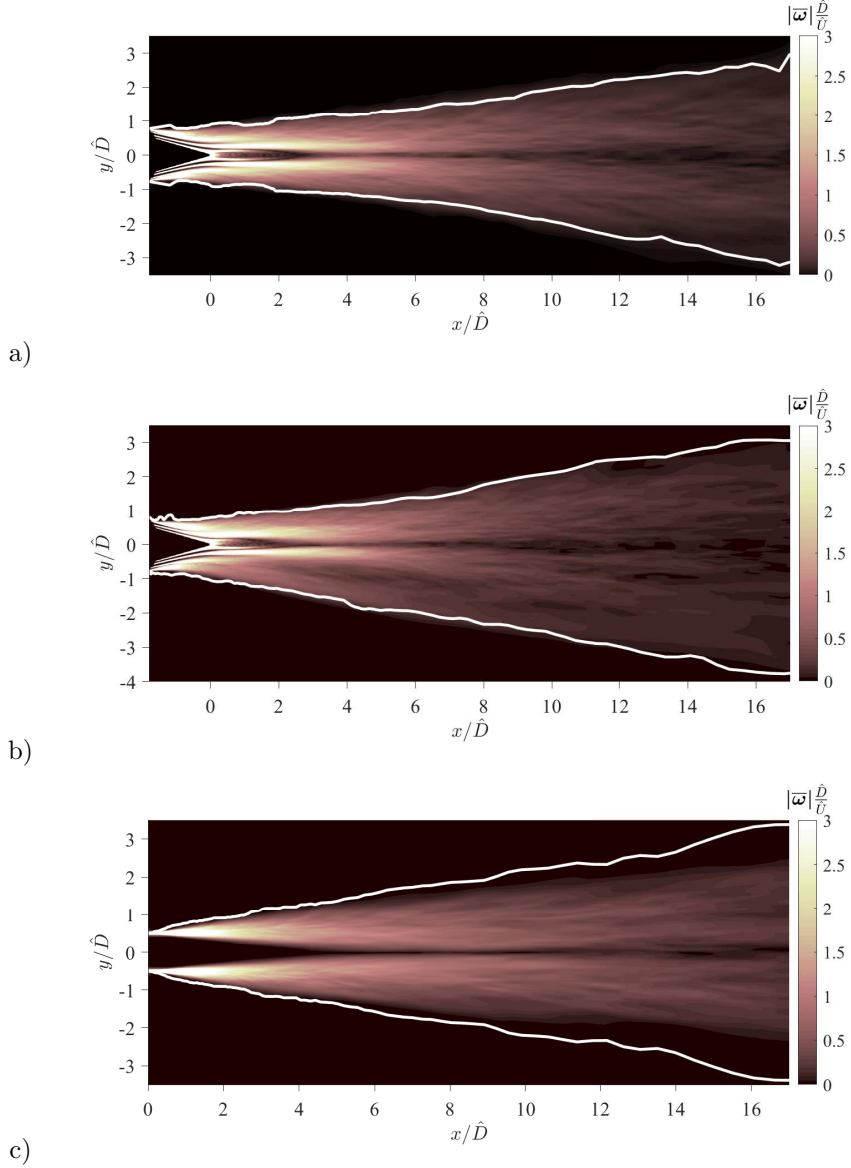
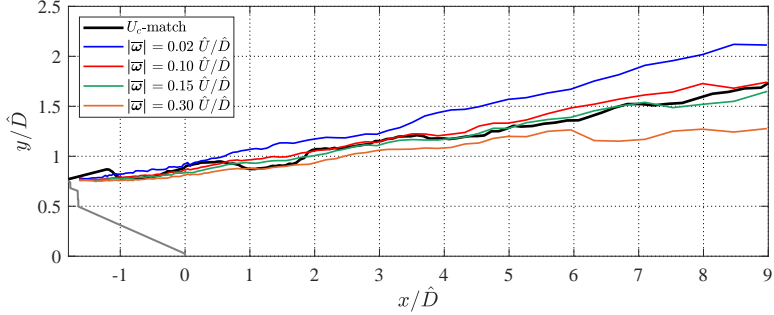


Figure 18: Distribution of $|\bar{\omega}|$ on the symmetry planes of jets: a) AXI04U; b) ECC09U; c) M09. White line: radiator surface based on U_c -match criterion.

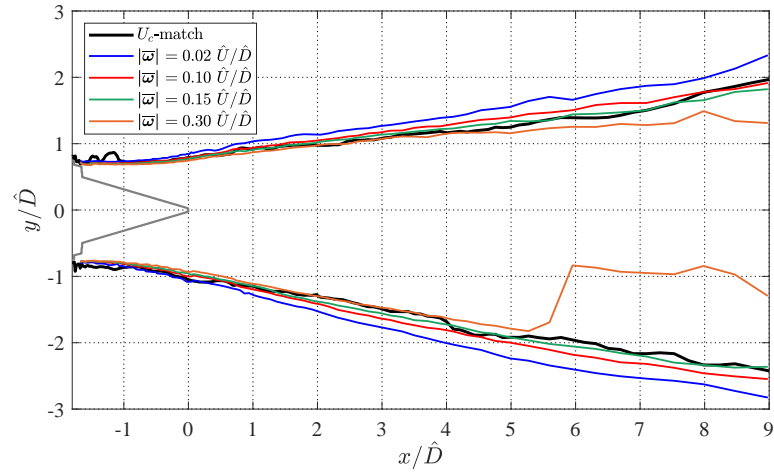
The above results motivate a simple criterion for locating the radiator surface based on a mean vorticity threshold. Although consistent with the physical motivation for Eq. 7, it would in fact be a much simpler criterion that does not require resolution of the outermost maximum gradient in the flow. In the following, we will compare the locations of surfaces of constant mean vorticity, using various thresholds of $|\bar{\omega}|\hat{D}/\hat{U}$, to the location of the radiator surface defined by the U_c -match procedure.

Figure 19 plots the location of surfaces of constant $|\bar{\omega}|\hat{D}/\hat{U}$ and the radiator surface on the symmetry plane of jets AXI04U, ECC09, and M09. It is seen that the mean-vorticity isosurfaces with threshold $|\bar{\omega}|\hat{D}/\hat{U} = 0.15$ come very close to the location of the radiator surface for the three-stream jets. For the single-stream jet M09, this threshold provides a good match in the potential core region $x/\hat{D} \leq 5$ but underpredicts moderately the radial location of the radiator surface past this region. Nevertheless,

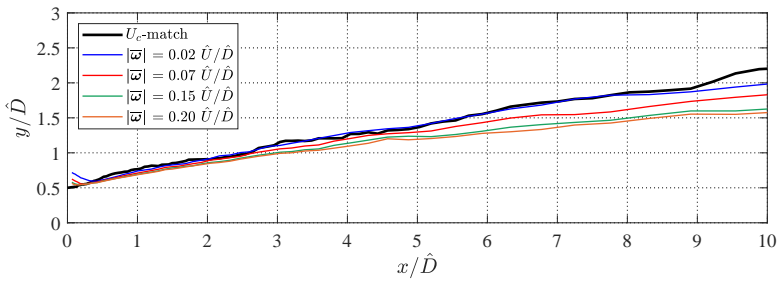
it is notable that the same criterion gives similar results in complex multi-stream jets and in the simple single-stream jet. To gain additional insight into the validity of the mean-vorticity criterion, we examine cross-sectional distributions for jet ECC09U in Fig. 20. The eccentricity of the radiator surface is noted. Once again the criterion $|\bar{\omega}| \hat{D}/\hat{U} = 0.15$ gives a surface that is very close to the radiator surface. It is also apparent from the above results that the locations of the mean-vorticity isosurfaces are not very sensitive on the threshold chosen as long as it is in the range $0.1 - 0.2$.



a)



b)



c)

Figure 19: Comparison of U_c -match radiator surface with surfaces of constant $|\bar{\omega}|$ on the symmetry plane of jets: a) AXI04U; b) ECC09U; c) M09.

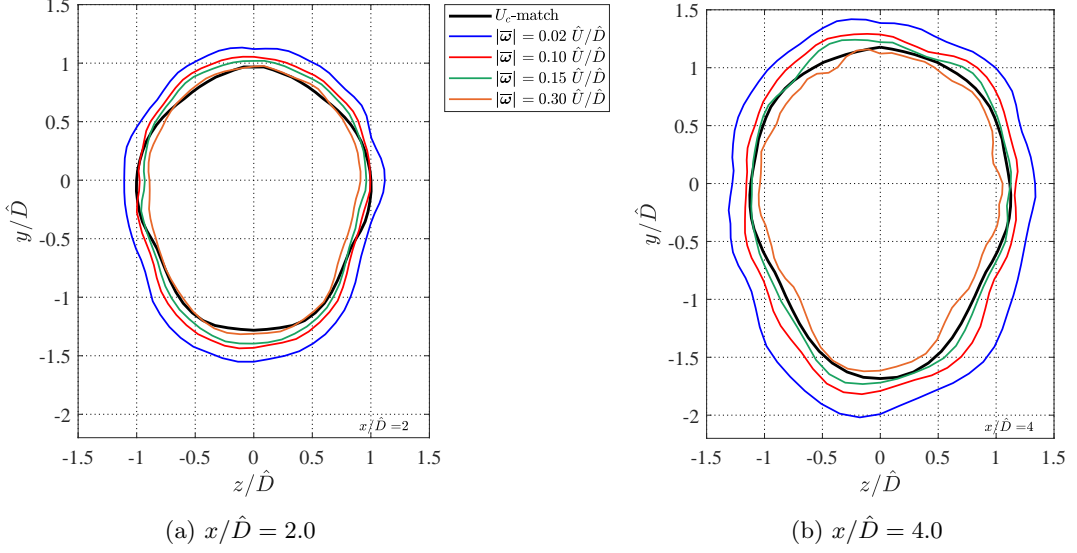


Figure 20: Comparison of U_c -match radiator surface with surfaces of constant $|\bar{\omega}|$ on two cross-sectional planes of jet ECC09U.

For a more quantitative evaluation of the mean vorticity threshold that produces a surface as close as possible to the radiator surface, we define the following root-mean-squared (rms) error between the relative locations of the two surfaces:

$$\chi = \sqrt{\frac{1}{x_2 - x_1} \frac{1}{2\pi} \int_{x_1}^{x_2} \int_0^{2\pi} \left[1 - \frac{r_\omega(x, \phi)}{r_{\text{RAD}}(x, \phi)} \right]^2 d\phi dx} \quad (8)$$

where r_{RAD} and r_ω are the radial locations of the radiator and equal-mean-vorticity surfaces, respectively. The integration limits x_1 and x_2 cover the region where the LES-based statistics are reliable and coincide with the range depicted in Fig. 19. Equation 10 is evaluated for a wide range of $|\bar{\omega}| \hat{D}/\hat{U}$, each producing a different distribution of r_ω . The results are shown in Fig. 21. As anticipated from the previous figures, thresholds near $|\bar{\omega}| \hat{D}/\hat{U} = 0.15$ minimize the error between the two surfaces, as low as 5%, for jets AXI04U and ECC09U. For jet M09, the threshold $|\bar{\omega}| \hat{D}/\hat{U} = 0.15$ gives a discrepancy of 15 %, which is considered moderate. For this jet, the error is minimized at the threshold $|\bar{\omega}| \hat{D}/\hat{U} = 0.02$.

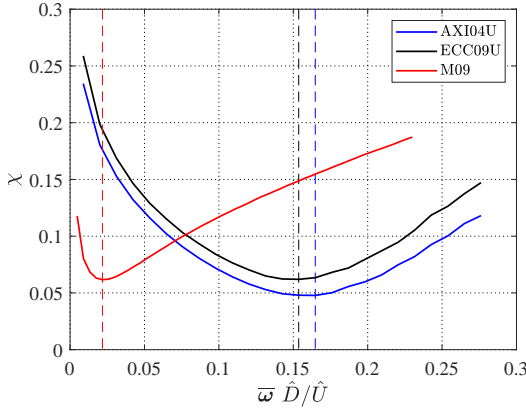


Figure 21: Relative deviation between U_c -match and surfaces based on constant mean vorticity. Dashed lines indicate the abscissa of the curve minimum.

D. Events Near the Jet Edge

To gain further insights as to the connection between events on the OSPS and their imprint on the radiator surface, we examine statistics and instantaneous phenomena near the edge of the jet. We start by examining the normalized skewness of the pressure

$$Sk\{p\} = \frac{\langle p'^3 \rangle}{\langle p'^2 \rangle^{3/2}} \quad (9)$$

An intriguing finding of recent experimental studies on the near pressure field of single- and dual-stream jets is the existence of a layer of negative skewness near the edge of the jet.³³ This has also been observed in LES of supersonic single-stream jets³⁵ as well as LES of jet AXI04U.²¹ We can thus state with confidence that it is an inherent feature of turbulent jets, at least in the high-speed regime. In Ref. 33 it was noted that the RANS-based radiator surface, defined according to the criterion of Eq. 7, was close to the locus of $Sk\{p\} \approx -0.3$. This motivates the question as to how the radiator surface and the negative skewness layer might be related.

Figure 22 plots isocontours of $Sk\{p\}$ for the jets of this study and includes the locations of the radiator surface. For all the jets, it is seen that the radiator surface is very close to or inside the layer of negative skewness that forms near the edge of the jet.

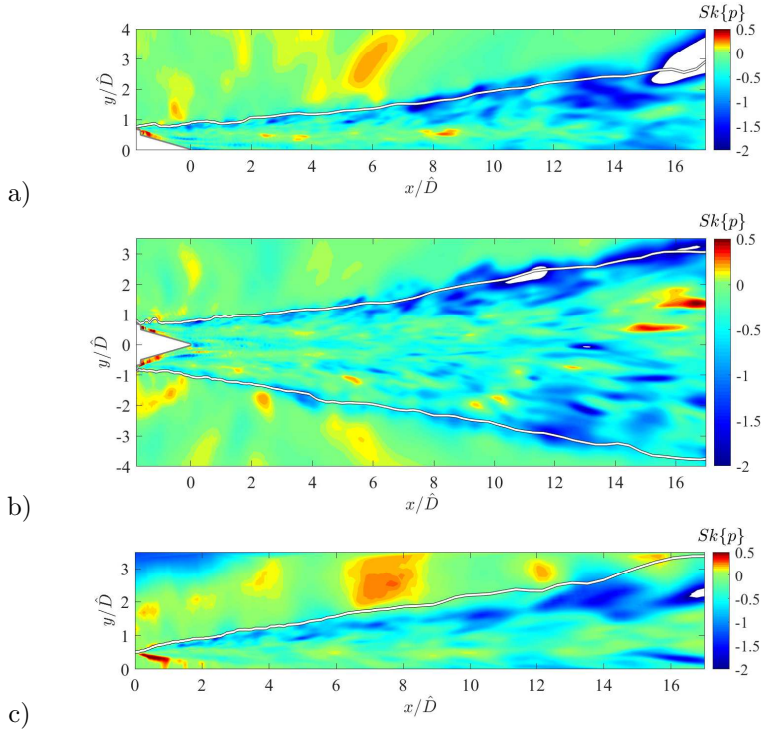


Figure 22: Distribution of the normalized skewness of the LES pressure field for jets: a) AXI04U (meridional plane); b) ECC09U (symmetry plane); c) M09 (meridional plane). White lines: radiator surface based on U_c -match criterion

To investigate further the origin of the layer of negative pressure skewness, we study instantaneous events in the vicinity of the radiator surface of jet AXI04U. We first examine the time evolution of the pressure at $x/\hat{D}=6.0$ and $\phi = 0^\circ$, a location where $Sk\{p\} = -0.6$ (Fig. 22(a)). A short segment of this evolution is plotted in Fig. 23, where p' is normalized by $p'_{rms,max}$, the maximum rms pressure fluctuation on the plane $\phi = 0^\circ$. We note a very strong negative peak at $t\hat{U}/\hat{D}=34$, which reaches $p'/p_{rms,max} = -0.6$. It is surmised that events like this sudden expansion contribute to the negative skewness.

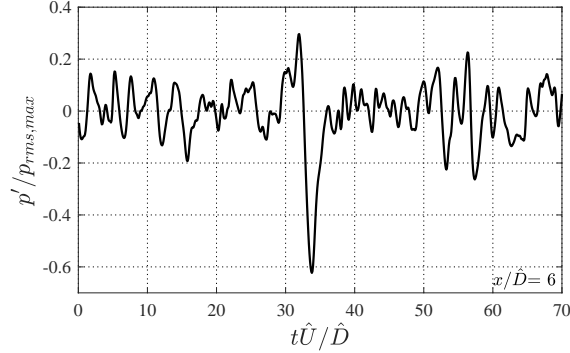


Figure 23: Pressure time history on the radiator surface of jet AXI04U at $x/\hat{D} = 6$ and $\phi = 0^\circ$.

Figure 24 shows the contour of instantaneous pressure fluctuation at the time of the sudden expansion noted in Fig. 23. It is seen that the cause of the intense negative peak is a localized pressure drop. The arrows in Fig. 24 denote the projection of the instantaneous velocity fluctuation vector on the plane $\phi = 0^\circ$ and help identify this event as a vortex rotating clockwise. The pressure drop is thus connected to the core of the vortex. The associated fluctuating vorticity is seen in the snapshot of ω'_z in Fig. 17, which is at the same time as the snapshot of Fig. 24. The negative vorticity blob seen grazing the radiator surface near $x/\hat{D} = 6$, $y/\hat{D} = -1.2$ in Fig. 17 is thus associated with the sharp expansion noted in Figs. 23 and 24. Further examination of Fig. 17 reveals similar vortical structures, with $\omega'_z > 0$, near the radiator surface at $\phi = 180^\circ$ (top side) near $x/\hat{D}=1.0$ and $x/\hat{D}=5.5$. Analogous analysis of these and similar events show associated negative pressure spikes. These observations suggest that the edge of the jet is affected by sparse vortices peeling off from the flow eddies and drifting towards the radiator surface. Their effects are imprinted as layers of negative pressure skewness. It is also possible that they contribute to the mechanism by which the convective velocity information on the OSPS (i.e., the location of the most energetic eddies) is transmitted to the radiator surface. These events constitute the last remnants of the vortical field and vanish outside the radiator surface, as is evident in Fig. 17.

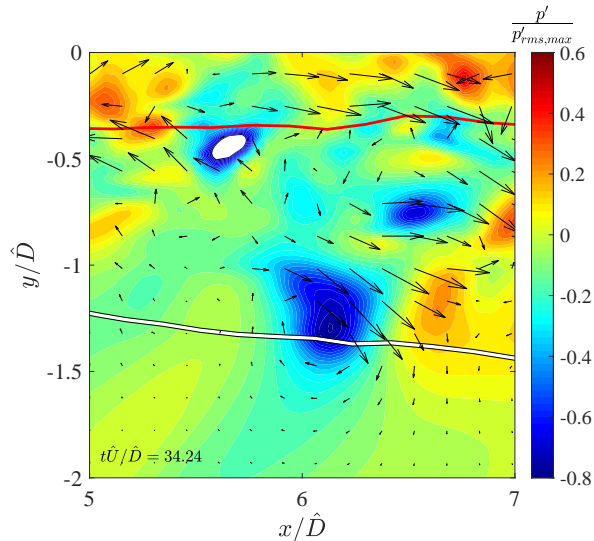


Figure 24: Contour of the instantaneous pressure fluctuation in jet AXI04U at $\phi = 0^\circ$. Arrows: projection of velocity fluctuation vectors on $x - y$ plane; white line: radiator surface based on U_c -match criterion; red line: OSPS surface based on LES.

VII. Concluding Remarks

We used Large Eddy Simulations (LES) of three different jets to assess key assumptions in the development of linear-based models for the noise source that would be informed by low-cost, RANS computations of the flow field. The simulations encompassed two triple-stream jets, one coaxial and the other eccentric, and a single-stream round jet. The three-stream jets exhausted at conditions simulating the takeoff set point of a supersonic turbofan engine, while the single-stream jet was cold and high-subsonic. Direct evaluation of the Reynolds stress and convective velocity U_c from the LES show good agreement with the RANS-based modeled values in the three-stream jets. This suggests the validity of modeling the convective velocity of the noise-generating turbulent as the mean axial velocity on the outer surface of peak stress (OSPS).

In addition, the LES results help define a “radiator surface” on which the jet noise source model would be prescribed. The radiator surface is located at the boundary between the rotational and irrotational field and is defined as the surface on which the U_c distribution, obtained from space-time correlations of the pressure, matches that inferred from the RANS model. This surface overlaps with a band of negative skewness of the pressure. Examination of the instantaneous vorticity field shows vortices peeling off from the main flow and migrating towards the radiator surface outside of which their strength vanishes. The vortical events near the radiator surface help explain the negative pressure skewness.

The edge of the mean vorticity field appears to coincide with the location of the radiator surface on the three-stream jets, which suggests a straight-forward RANS-based criterion for locating this surface. Specifically, surfaces of $|\bar{\omega}| = 0.15 \hat{U}/\hat{D}$ come very close to the radiator surface as defined by the U_c -match criterion. In terms of the ultimate predictive scheme illustrated in Fig. 1, small errors in the location of the radiator surface are unlikely to have significant impact on the accuracy of the propagated and scattered acoustic fields. Instead, one of the most critical elements of the prediction method is the convective velocity of the partial fields, which this research effort indicates can be modeled with reasonable accuracy using RANS.

References

- ¹Brès, G., Ham, F., Nichols, J., and Lele, S., “Unstructured Large-Eddy Simulations of Supersonic Jets,” *AIAA Journal*, Vol. 55, No. 4, 2017.
- ²Henderson, B., “Aeroacoustics of Three-Stream Jets,” *AIAA Paper 2012-2159*, June 2012.
- ³Henderson, B., Leib, S., and Wernet, M., “Measurements and Predictions of the Noise from Three-Stream Jets,” *AIAA Paper 2015-3120*, Jan. 2015.
- ⁴Henderson, B. and Wernet, M., “Measurements and Predictions of the Noise from Three-Stream Jets,” *NASA/TM-2016-219098*, July 2016.
- ⁵Huff, D. and Henderson, B., “The Aeroacoustics of Offset Three-Stream Jets for Future Commercial Supersonic Aircraft,” *AIAA Paper 2016-2992*, June 2016.
- ⁶Papamoschou, D., Phong, V., Xiong, J., and Liu, F., “Quiet Nozzle Concepts for Three-Stream Jets,” *AIAA Paper 2016-0523*, Jan. 2016.
- ⁷Phong, V. and Papamoschou, D., “Investigation of Isolated and Installed Three-Stream Jets from Offset Nozzles,” *AIAA Paper 2017-0005*, Jan. 2017.
- ⁸Leib, S., “Modeling Sound Propagation Through Non-Axisymmetric Jets,” *NASA/CR-2014-218107*, March 2014.
- ⁹Papamoschou, D., “Modelling of Noise Reduction in Complex Multistream Jets,” *Journal of Fluid Mechanics*, Vol. 834, Jan. 2018, pp. 555–599.
- ¹⁰Ffowcs Williams, J. and Hawkings, D., “Sound Generation by Turbulence and Surfaces in Arbitrary Motion,” *Philosophical Transactions of the Royal Society A*, Vol. 264, No. 1151, 1969, pp. 321–342.
- ¹¹Pilon, A. and Lyrintzis, A., “Development of an Improved Kirchhoff Method for Jet Aeroacoustics,” *AIAA Journal*, Vol. 36, No. 5, 1998, pp. 783–790.
- ¹²Papamoschou, D., “Prediction of Jet Noise Shielding,” *AIAA Paper 2010-0653*, June 2010.
- ¹³Papamoschou, D. and Mayoral, S., “Modeling of Jet Noise Sources and their Diffraction with Uniform Flow,” *AIAA Paper 2013-0326*, Jan. 2013.
- ¹⁴Ho, C., “Near Field Pressure Fluctuations in a Circular Jet,” *NASA CR-179847*, Nov. 1985.
- ¹⁵Zaman, K., “Flow Field and Near and Far Sound Field of a Subsonic Jet,” *Journal of Sound and Vibration*, Vol. 106, No. 1, 1986, pp. 1–16.
- ¹⁶Morris, P., “A Note on Noise Generation by Large Scale Turbulent Structures in Subsonic and Supersonic Jets,” *International Journal of Aeroacoustics*, Vol. 8, No. 4, 2009, pp. 301–316.
- ¹⁷Reba, R., Narayanan, S., and Colonius, T., “Wave-Packet Models for Large-Scale Mixing Noise,” *International Journal of Aeroacoustics*, Vol. 9, 2010, pp. 533–558.
- ¹⁸Papamoschou, D., “Wavepacket Modeling of the Jet Noise Source,” *AIAA Paper 2011-2835*, June 2011.
- ¹⁹Jordan, P. and Colonius, T., “Wave Packets and Turbulent Jet Noise,” *Annual Review of Fluid Mechanics*, Vol. 45, 2013, pp. 173–195.

- ²⁰Papamoschou, D., "On the Connection Between Near and Far Pressure Fields of a Turbulent Jet," *AIAA Paper 2018-1251*, Jan. 2018.
- ²¹Adam, A., Papamoschou, D., Xiong, J., and Liu, F., "The Very Near Pressure Field of Three-Stream Jets," *AIAA Paper 2018-1739*, Jan. 2018.
- ²²Xiong, J., Johnson, A., Liu, F., and Papamoschou, D., "Body Force Model for the Aerodynamics of Inclined Perforated Surfaces," *AIAA Journal*, Vol. 50, No. 11, 2012, pp. 2525–2535.
- ²³Jameson, A., Schmidt, W., and Turkel, E., "Numerical Solutions of the Euler Equations by Finite Volume Methods Using Runge-Kutta Time Stepping Schemes," *AIAA Paper 1981-1259*, Jan. 1981.
- ²⁴Menter, F., "Two-Equation Eddy-Viscosity Turbulence Models for Engineering Applications," *AIAA Journal*, Vol. 32, No. 8, 1994, pp. 1598–1605.
- ²⁵Xiong, J., Nielsen, P., Liu, F., and Papamoschou, D., "Computation of High-Speed Coaxial Jets with Fan Flow Deflection," *AIAA Journal*, Vol. 48, No. 10, 2010, pp. 2249–2262.
- ²⁶Roe, P. L., "Approximate Riemann Solvers, Parameter Vectors and Difference Schemes," *Journal of Computational Physics*, Vol. 46, No. 2, 1980, pp. 357–378.
- ²⁷Shur, M. L., Spalart, P. R., and Strelets, M. K., "Noise Prediction for Increasingly Complex Jets. Part I: Methods and Tests," *International Journal of Aeroacoustics*, Vol. 4, No. 3, 2005, pp. 213–246.
- ²⁸Spalart, P. R., Jou, W. H., Strelets, M., and Allmaras, S. R., "Comments on the Feasibility of LES for Wings, and on a Hybrid RANS/LES Approach," 1st AFOSR Int. Conf. on DNS/LES, Ruston, LA, August 1997.
- ²⁹Spalart, P. R. and Allmaras, S. R., "A One-Equation Turbulence Model for Aerodynamic Flows," *AIAA Paper 1992-0439*, January 1992.
- ³⁰Papamoschou, D. and Rostamimonjezi, S., "Effect of Velocity Ratio on Noise Source Distribution of Coaxial Jets," *AIAA Journal*, Vol. 48, No. 7, 2010, pp. 1504–1512.
- ³¹Papamoschou, D., "Modeling of Noise Reduction in Complex Multistream Jets," *AIAA Paper 2017-0001*, Jan. 2017.
- ³²Bridges, J., "Effect of Heat on Space-Time Correlations in Jets," *NASA/TM-2006-214381*, September 2006.
- ³³Papamoschou, D. and Phong, V., "The Very Near Pressure Field of Single- and Multi-Stream Jets," *AIAA Paper 2017-0230*, Jan. 2017.
- ³⁴Papamoschou, D., Xiong, J., and Liu, F., "Towards a Low-Cost Wavepacket Model of the Jet Noise Source," *AIAA Paper 2015-1006*, Jan. 2015.
- ³⁵Pineau, P. and Bogey, C., "Study of the Generation of Shock Waves by High-Speed Jets Using Conditional Averaging," *AIAA Paper 2018-3305*, June 2018.